

# High-resolution friction force microscopy under electrochemical control

Aleksander Labuda,<sup>1</sup> William Paul,<sup>1</sup> Brendan Pietrobon,<sup>2</sup> R. Bruce Lennox,<sup>2</sup> Peter H. Grütter,<sup>1</sup> and Roland Bennewitz<sup>1,3</sup><sup>1</sup>*Department of Physics, McGill University, Montreal, Quebec H3A 2T8, Canada*<sup>2</sup>*Department of Chemistry, McGill University, Montreal, Quebec H3A 2K6, Canada*<sup>3</sup>*INM—Leibniz Institute for New Materials, 66123 Saarbrücken, Germany*

(Received 11 May 2010; accepted 5 July 2010; published online 2 August 2010)

We report the design and development of a friction force microscope for high-resolution studies in electrochemical environments. The design choices are motivated by the experimental requirements of atomic-scale friction measurements in liquids. The noise of the system is analyzed based on a methodology for the quantification of all the noise sources. The quantitative contribution of each noise source is analyzed in a series of lateral force measurements. Normal force detection is demonstrated in a study of the solvation potential in a confined liquid, octamethylcyclotetrasiloxane. The limitations of the timing resolution of the instrument are discussed in the context of an atomic stick-slip measurement. The instrument is capable of studying the atomic friction contrast between a bare Au(111) surface and a copper monolayer deposited at underpotential conditions in perchloric acid. © 2010 American Institute of Physics. [doi:10.1063/1.3470107]

## I. INTRODUCTION

Friction force microscopy is the most important method for the investigation of fundamental concepts in the field of tribology by probing sliding contacts on a nanometer scale. It provides straightforward results for a single asperity contact while studies of macroscopic systems are usually complicated by the interdependent action of a large ensemble of microscopic contacts. Three of many examples which demonstrate the power of friction force microscopy are the observation of atomic friction phenomena,<sup>1</sup> the determination of the velocity dependence of friction for hydrophilic and hydrophobic sample surfaces,<sup>2</sup> and the confirmation of the concept of ultralow friction in noncommensurate contacts.<sup>3</sup>

Here we report on the development of an instrument dedicated to high-resolution force microscopy in an electrochemical cell. This environment allows the study of friction and wear on surfaces which are modified *in situ* by variation of the electrochemical potential or by variation of the electrolyte. The modifications include oxidation and reduction of surfaces, deposition of ultrathin films, and the controlled adsorption of molecular layers. Earlier work has addressed frictional changes at steps on graphite upon changing the electrochemical potential.<sup>4</sup> Recent reports have shown how the deposition of copper as well as the adsorption of anions on a Au(111) electrode modify the friction behavior at the nanometer scale.<sup>5,6</sup>

This report starts with a description of the instrumental design optimized for detection of atomic friction phenomena. The design criteria focus on the noise minimization in this particular mode of measurement. Then, the noise of the instrument is characterized with respect to detection sources and mechanical sources. The performance of the instrument is demonstrated on a series of measurements of lateral force on Au(111) and of normal forces on confined liquid layers of octamethylcyclotetrasiloxane (OMCTS). Finally, we study

the difference in atomic friction between Au(111) and the same surface immediately after copper underpotential deposition (Cu UPD) in perchloric acid.

## II. DESIGN

The noise sources of an atomic force microscope (AFM) can be divided into three categories: mechanical noise between the imaging tip and sample, detection noise (detection of tip movement), and feedback noise. The final AFM topography signal is corrupted by a combination of all three because the feedback loop transduces its own noise and the detection noise into a physical tip-sample movement. As such, standard topographic AFM imaging relies on a rigid tip-sample connection, low-noise detection of the cantilever deflection, and an optimized feedback system to ensure accurate sample topography tracking. However, requirements for high-resolution friction force microscopy are different: lateral force data is recorded in a quasi-constant-height mode where a slow feedback only corrects for slow drift of the instrument and sample tilt. Using a slow feedback loop on atomically flat surfaces avoids cross-talk between lateral force modulations and topographic feedback, reduces feedback noise, and effectively decouples the mechanical and detection noise sources. Mechanical noise can severely disrupt friction mechanisms; for example, the enabling and disabling of the atomic stick-slip mechanism through resonant excitation of the cantilever.<sup>7</sup>

These considerations shift the design paradigm toward minimizing mechanical noise at the potential expense of increased detection noise and drift. This is achieved by mechanically decoupling the detection components from the mechanical assembly joining the sample and cantilever to increase its rigidity and resonance frequency. Furthermore, distancing the detection components leaves more room for a

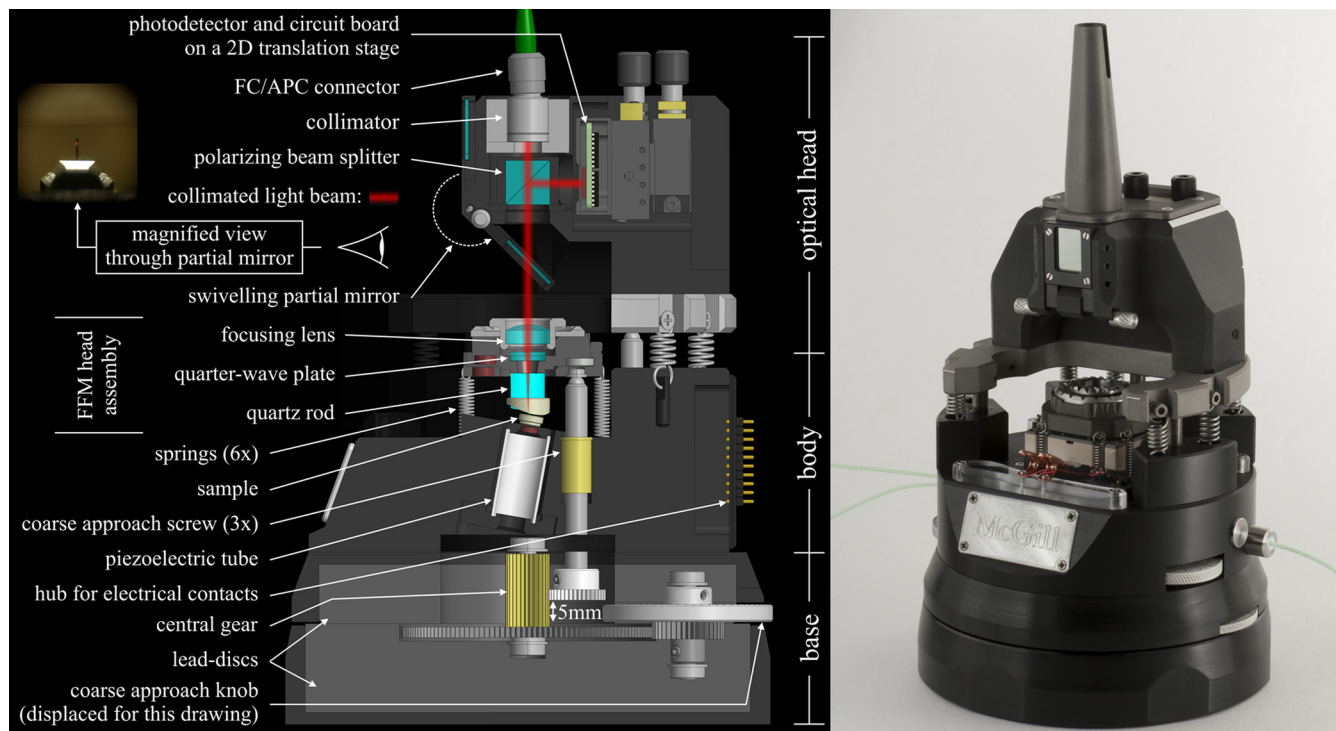


FIG. 1. (Color online) Photograph of the friction force microscope, side-view technical drawing illustrating the details of the three main parts: body, base, and optical head. A magnified view of the cantilever and focused light spot is seen after lowering the partial mirror.

large and rigid liquid cell whose fluid lines and electrical wires transfer less mechanical vibrations to the imaging environment.

### A. Overview

The stiff and symmetric design of this friction force microscope (FFM) intends to reduce mechanical vibrations, external noise coupling, and drift. The structural components of the FFM are mostly built from aluminum because it offers a compromise between the desire for high stiffness, low density, and easy machinability. The high thermal conductivity promotes fast thermal equilibration, which offsets the problematically high thermal coefficient of expansion. Figure 1 shows a side cut of the FFM which depicts its three main parts: the *body*, the *base*, and the *optical head*. In the remainder of the text, italic words refer to figure labels.

The body supports the crucial components for stable imaging: the *piezoelectric tube scanner*, *FFM head assembly*, and electrochemical (EC) cell (not shown in Fig. 1 for clarity). The piezoelectric tube moves the *sample* within a  $6\ \mu\text{m} \times 6\ \mu\text{m} \times 3\ \mu\text{m}$  scan range controlled by voltages in the range  $\pm 135\ \text{V}$ , while the FFM head assembly holds the cantilever. It sits on three *coarse-approach screws* (1/4 in.-80TPI), while six *springs* hold it down with a total force of  $\sim 20\ \text{N}$ . These three screws are equidistant to a long *central gear* which moves them synchronously with a full range of 5 mm in the *z*-direction and are geared down to a manual resolution of roughly  $1\ \mu\text{m}$ . Ball bearings ensure frictionless rotation between the screws and the FFM head assembly. The intended application of this FFM—nanometer-scale friction—warrants the absence of any lateral coarse positioning mechanism.

The 5 kg lead-filled base supports the body and houses the coarse-approach gearing. The design ensures that the FFM is mechanically coupled to the table solely through two 2 cm thick *lead disks*—with the exception of electrical and fluidic contacts which are rigidly fastened to the body before reaching the imaging components. Lead was chosen for its high-damping properties and its acoustic mismatch with aluminum. An active isolation table (TS-150, Table Stable) further reduces the effects of table and building vibrations.

The optical head's purpose is the detection of the cantilever bending using the optical beam deflection (OBD) method.<sup>8</sup> A four-quadrant *photodetector* (S5980, Hamamatsu) detects the normal and lateral deflection of the cantilever by a change in the position of the *collimated light beam* reflected from the cantilever. The incoming and outgoing light beams are separated by the *polarizing beam splitter* with the help of the mica *quarter-wave plate*. This polarization method, described by Schaffer *et al.*,<sup>9</sup> was adopted to allow for a compact design and to simplify machining, albeit at the expense of more intricate optics. Mechanically decoupling the optical head components from the FFM head assembly prevents the mass loading of the tip-sample mechanical junction, as seen in Fig. 1. This provides the latter with a high resonance frequency, which reduces external noise coupling.<sup>10</sup>

A 1 mW superluminescent diode (SLD-261-MP1, Superlum) with wavelength centered at 680 nm and a bandwidth of 10 nm creates the light necessary for OBD scheme. The wide bandwidth shortens the coherence length to  $\sim 50\ \mu\text{m}$ , which reduces optical feedback noise and interference noise—both caused by reflections from optical components and the sample surface. The light beam enters a 2 mm *colli-*

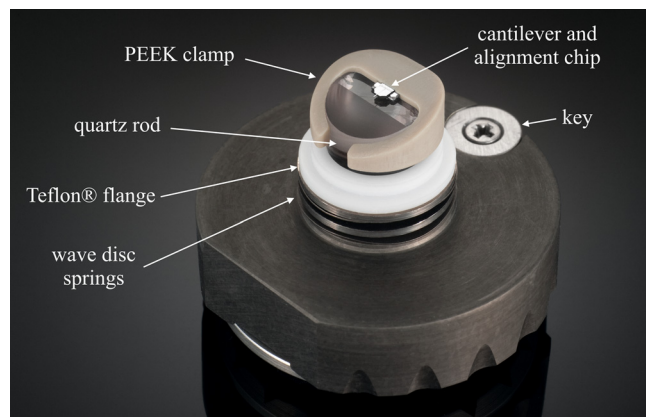


FIG. 2. (Color online) FFM head, upside down. The PEEK clamp anchors the cantilever to the quartz rod without the use of any metal components. The wave disk springs apply a force onto the Teflon® flange which seals the liquid cell. For a technical drawing of the other components of the FFM head refer to Fig. 3.

ator via a polarization maintaining single-mode fiber and *FC/APC* connector. This light beam is then focused through a 19 mm focal length *lens* (Thorlabs) onto the cantilever, leading to a diffraction limited spot of 8  $\mu\text{m}$  in diameter. The optical head itself is a two-dimensional tilt-stage used to center the focused spot on the cantilever tip: the focusing lens in the FFM head acts like an optical lever by converting the angle of the light beam into a position of the focused spot. Lowering the *partial mirror* gives a *magnified view* of the tip and focused spot to aid their alignment. The sample and tip can be illuminated by a miniature light-emitting diode embedded in the EC cell wall.

## B. FFM head

Figure 2 shows an upside-down photograph of the *FFM head*, which supports the *cantilever*. The *quartz rod* extends the FFM head into the liquid environment and guides the light beam onto the cantilever. Quartz was chosen due to availability, transparency at 680 nm and electrochemical inertness. The cantilever is fitted into a Nanosensors™ alignment chip before being slid into the *polyether ether ketone* (PEEK) clamp, which grips the quartz rod and rigidly sandwiches the cantilever in place. The chromium coating on the alignment chip was chemically stripped.

Figure 3 shows a technical drawing of the FFM head, which slides into the *FFM head housing* via a *keyway* mechanism and locks into place by the torque of six pairs of NdFeB magnets. It remains magnetically spring-loaded throughout the operation of the instrument. With alignment repeatability better than 10  $\mu\text{m}$  with respect to the light beam, the FFM head can be quickly removed and replaced without the need to recenter the light beam onto the cantilever. Note that quartz, PEEK, and the silicon oxide of the cantilever assembly are the only materials in contact with the electrolyte.

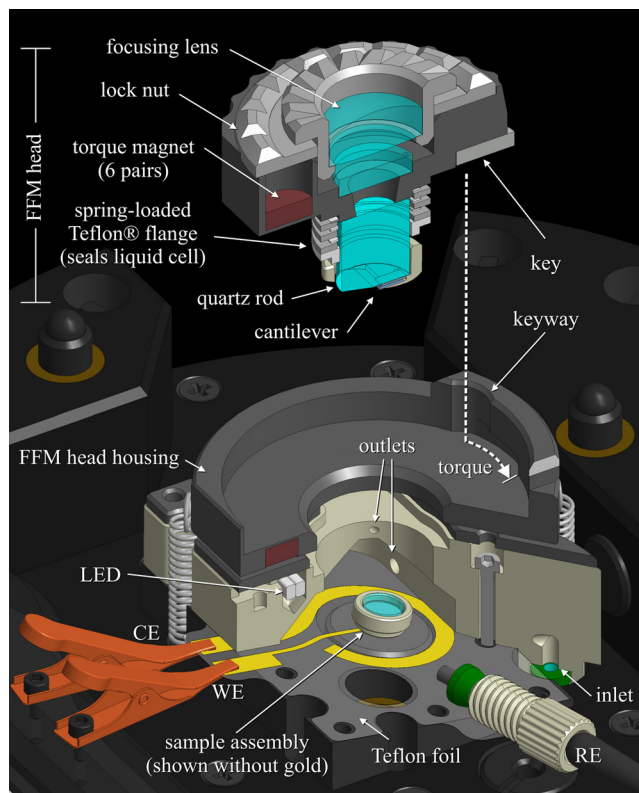


FIG. 3. (Color online) Technical drawing of the electrochemical cell and FFM head combination. The counter and working electrodes (CE and WE) are gold-sputtered onto the Teflon® film, while the reference electrode (RE) is a Ag/AgCl electrode.

## C. Electrochemical cell

The EC cell design is strongly influenced by the choice of scanner used for sample positioning. Here, a five-electrode piezoelectric tube was chosen because of its compact size. To avoid accidentally shorting the high-voltage piezoelectric tube, many AFM designs keep the tube above the EC cell and consequently scan the cantilever rather than the sample. Two problems arise: either the cantilever moves under a fixed light beam, mixing the scanning motion into the OBD signal, or the piezoelectric tube moves all the necessary optics together, thus greatly lowering the resonance frequency of the scanner. The latter option reduces the maximum imaging speed and increases external noise coupling.<sup>10</sup>

This design with a scanned sample and stationary cantilever is depicted in the technical drawing in Fig. 3 and photographs in Fig. 4. A 50  $\mu\text{m}$  Teflon® film [DuPont™, perfluoroalkoxy (PFA)] seals the bottom of the EC cell, which is mounted on the body. When a sample is introduced into the EC cell, it firmly attaches to the piezoelectric tube that is beneath this Teflon® film by magnetic force. Because the film is mechanically compliant, the piezoelectric tube can move the sample in three dimensions without moving the EC cell. This mechanical isolation avoids mass loading of the tube by the EC cell.

The stiffness of the Teflon® film applies a restoring force onto the piezoelectric tube which slightly increases its lateral resonant frequency. Introduction of water into the EC cell reduces the frequency to just below the free-standing frequency because of viscous drag on the sample. The Q-factor

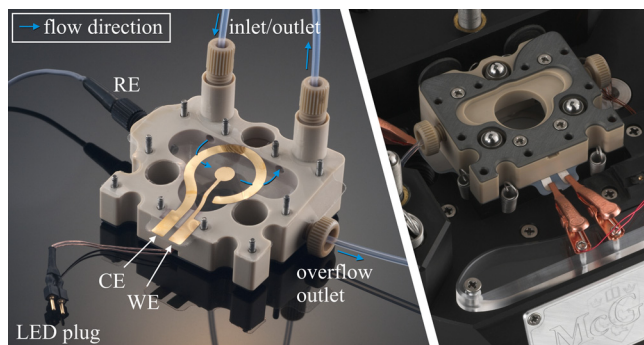


FIG. 4. (Color online) Left: upside down electrochemical cell (EC) with sealing Teflon<sup>®</sup> film. The reference, counter, and working electrodes are shown (RE, CE, and WE), as well as inlet and outlets for fluid flow. Right: mounted EC cell with FFM head assembly removed for visibility. Note the ball ends of the three equidistant coarse approach screws.

is also reduced. These changes in resonant frequency are small (<20%) compared to a design with a tube mass-loaded by an EC cell or optical components.

Another consequence of Teflon<sup>®</sup> film stiffness is the reduction of scan range. This effect can be greatly reduced by introducing a ring-shaped warping of the foil around the sample by means of mechanical indentation. In that case, the lateral scan range is reduced by less than 10%, whereas the vertical range remains unaffected. Nonlinearity, if any, caused by the Teflon<sup>®</sup> film is negligible compared to the intrinsic nonlinearity of the piezoelectric tube.

A relatively large volume of 2 ml was chosen for the EC cell to ensure a stable temperature and solution concentration throughout each experiment. Furthermore, a Teflon<sup>®</sup> flange on the FFM head seals the EC cell (as seen in Figs. 2 and 3) to prevent concentration and temperature gradients caused by electrolyte evaporation. The sealing pressure is provided by *wave disk springs* mounted around the quartz rod. The EC cell was machined out of PEEK to avoid ionic and organic contamination. As seen in Figs. 3 and 4, an *inlet/outlet* pair fills and drains the cell. It accesses the liquid cell from the bottom to reduce the turbulence of the liquid during transferring; this prevents the formation of microscopic air bubbles, caused by pouring the liquid, which are detrimental to OBD because of light scattering. An *overflow outlet*, near the top of the EC cell, prevents overflow and sets a consistent liquid level when filling the cell. The tubing has a 1 mm inner diameter and is made from Teflon<sup>®</sup> PFA. A peristaltic pump (Cole-Parmer) services all outlets simultaneously with a variable flow rate (0.2–1100 ml/min).

As seen in Fig. 3, a 10° tilt between the sample and cantilever is introduced for clearance while imaging. Tilting the sample instead of the cantilever greatly simplified the machining by keeping all optical components on one axis. In addition, it facilitates draining the EC cell due to its tilted floor.

For electrochemical control, the EC cell was fitted with a reference, counter, and working electrode (RE, CE, and WE, respectively). The RE is an Ag/AgCl reference electrode that is packaged in a 2 mm PEEK tube (World Precision Instruments). It accesses the cell through a nut and ferrule port (Upchurch) on the side of the EC cell. Access ports for the

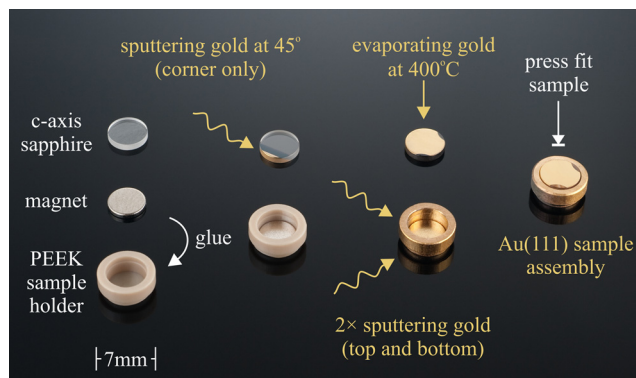


FIG. 5. (Color online) Sample manufacturing process. Sputtering gold on the sapphire edge before evaporation is necessary for electrical contact to the sample holder. The final sample assembly has a Au(111) top surface which is electrically connected to the bottom (<4  $\Omega$ ).

CE and WE were avoided by patterning the electrodes directly onto the Teflon<sup>®</sup> film. Alligator clips contact those electrodes which extend beyond the EC cell. Sputtering gold or platinum films onto Teflon<sup>®</sup> creates mechanically stable films; even after severe bending and rubbing during the cleaning process, the 100 nm films stay attached and maintain a constant low electrical resistance (<4  $\Omega$  for Au). The CE area is large to prevent limiting reaction rates, and it is radially symmetric around the sample (the WE) to provide homogenous electric fields at the sample surface. A potentiostat (CH Instruments, 1030 A) controls the electrochemical potentials.

#### D. Sample

All preliminary experiments were performed on an evaporated gold film, where friction experiments were carried out on atomically flat Au(111) terraces. Figure 5 illustrates the sample manufacturing process. A 100 nm layer of gold is evaporated on *c-axis sapphire* disks (Edmund Optics) using a commercial evaporator (Thermionics). Heating the substrate to 400 °C promotes the growth of large Au(111) oriented grains with flat terraces (up to 400 nm).<sup>11</sup> No adhesion layer is used to avoid electrochemical contamination of the liquid environment and ambiguity in data interpretation.

The *sample holder* is made of gold-sputtered (100 nm) PEEK and electrically connects the sample to the WE on the Teflon<sup>®</sup> film. Its task is depicted in Fig. 3. Press fitting the sample into the sample holder provides electrical contact and hermetically encapsulates the NdFeB magnet. The electrical resistance between the potentiostat and the Au(111) is below 10  $\Omega$ .

The drawback of this method is the dominating electrochemical signal from the large surface area of the sample holder. Figure 6 demonstrates that the sample is about seven times smaller than the sample holder and WE in effective surface area, and that the cyclic voltammogram of the polycrystalline gold sample holder exhibits a different electrochemical signature than the Au(111) sample.

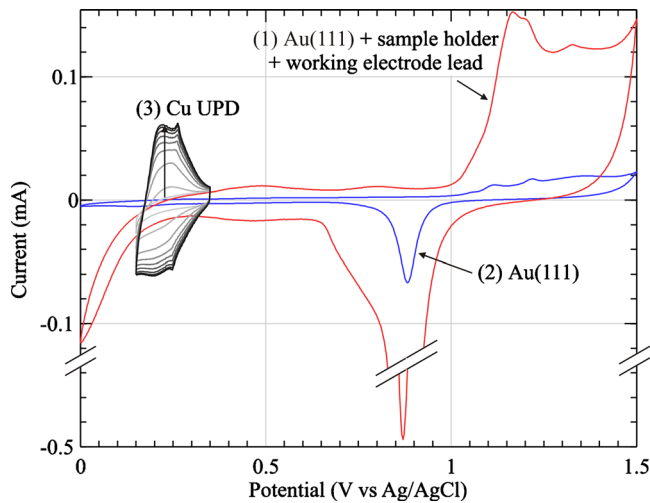


FIG. 6. (Color online) (1) Cyclic voltammogram (CV) of gold oxidation-reduction in 0.1 M HClO<sub>4</sub>+10<sup>-5</sup> M HCl during imaging. The reaction occurs at the Au(111) sample surface, the electrode lead, and the gold-sputtered sample holder. (2) CV of the isolated Au(111) sample surface. (3) CV taken during the pumping of extra solution with added 30 mM Cu<sup>2+</sup>. The progression in time is indicated by the arrow; it shows the increase in monolayer coverage of the Cu UPD. All CVs acquired at 20 mV/s.

### E. Cantilever

The cantilever (and tip) is the force transducer of the FFM for both lateral and normal forces. An applied lateral force to the tip transduces into a torsional bending of the cantilever; the torsional angle can be measured by the OBD system. The calibration factor, in units of N/rad, is given by the stiffness-length product  $hk_L$ , where  $h$  is the tip height and  $k_L$  is the lateral stiffness of the cantilever-tip transducer. Similarly, an applied normal force to the tip transduces into an angular deflection of the cantilever, which can be measured by the OBD system and calibrated using the stiffness-length product  $\frac{3}{2}lk_N$ , where  $l$  is the tip-to-base distance,  $k_N$  is the stiffness normal to the surface, and 3/2 is related to the geometry of cantilever bending.<sup>12</sup> It is desirable to keep these calibration factors small in order to obtain large angular deflections for small applied forces. It is important to note that the lateral and normal calibration factors are frequency dependent, and can only be considered constant below the first respective resonance.

In the experiments presented here, the NanoSensors™ PPP-CONT cantilevers were used, with a nominal normal stiffness of 0.2 N/m and dimensions 450 μm × 50 μm × 2 μm. A reflective coating on the cantilevers was omitted for the risk of electrochemically induced stress in the coating, which would hamper the force detection. The cantilever is left electrically floating to avoid ohmic currents between the tip and the sample. Once in contact it follows the WE potential. Electrochemical reactions at the surface of the silicon cantilever are suppressed by the insulating native oxide.

The cantilever's normal and lateral stiffness values were determined using Sader's method based on thermal noise spectra of both normal and lateral deflections recorded in air.<sup>13,14</sup> They were imaged in a scanning electron microscope to obtain the parameters necessary for calibration:  $l$ ,  $h$ , and the cantilever length.

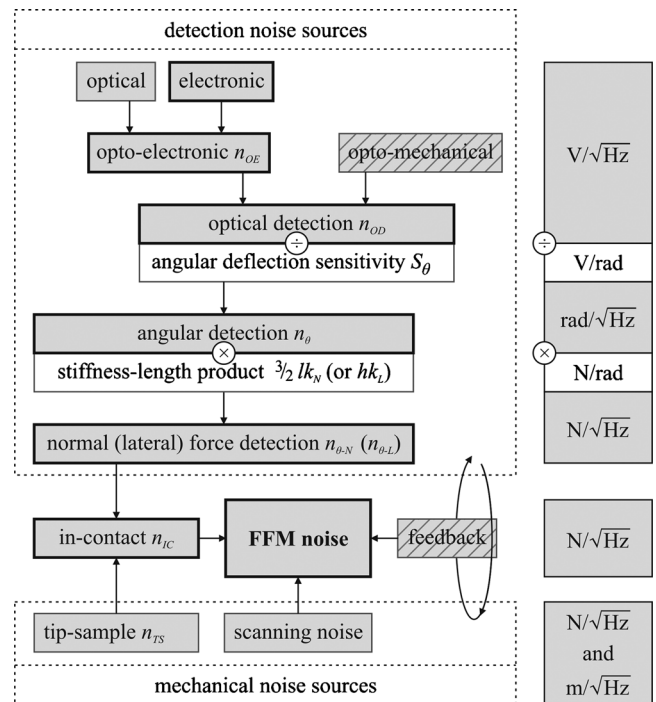


FIG. 7. Breakdown of mechanical and detection noise sources (gray boxes) and calibration factors (white boxes), which contribute to total FFM noise. The feedback noise is eliminated by imaging in quasiconstant height mode. The optomechanical noise is below the detection limit. Thick-border boxes indicate that the corresponding noise density is directly measurable experimentally; the rest are deduced by quadratic subtraction. The noise density units are indicated on the right. The mechanical noise sources have two units as they can originate from either forces applied to the cantilever or displacements of the sample or cantilever.

### III. NOISE AND PERFORMANCE

A thorough understanding of noise and its sources is important in the development of an FFM for atomic-scale resolution. The modulation of lateral forces by the atomic structure of the surfaces can be as low in amplitude as the thermal noise of the force sensor, and average lateral forces which reveal dissipation, and therefore friction, can be much smaller.<sup>15</sup> Correctly interpreting these signals requires detailed knowledge of the noise characteristics of the instrument.

The following section systematically quantifies the noise sources of this FFM. Figure 7 provides a road map for this entire analysis. As explained in the previous section, the *detection noise sources* and *mechanical noise sources* are decoupled by the low-passed feedback loop. This section starts with the detection noise of the optical beam deflection system; it is then followed by a characterization of the mechanical noise sources; and finally a comparative analysis of the influence of each source on various experiments.

#### A. High-bandwidth optical beam deflection system

The quality of optoelectronic detection relies on a compromise between low noise and high bandwidth. Optimal performance for the OBD electronics can be achieved by engineering a circuit with electronic noise just below that of the optical noise while maximizing the detection bandwidth. Even though the topographic feedback speed is limited by

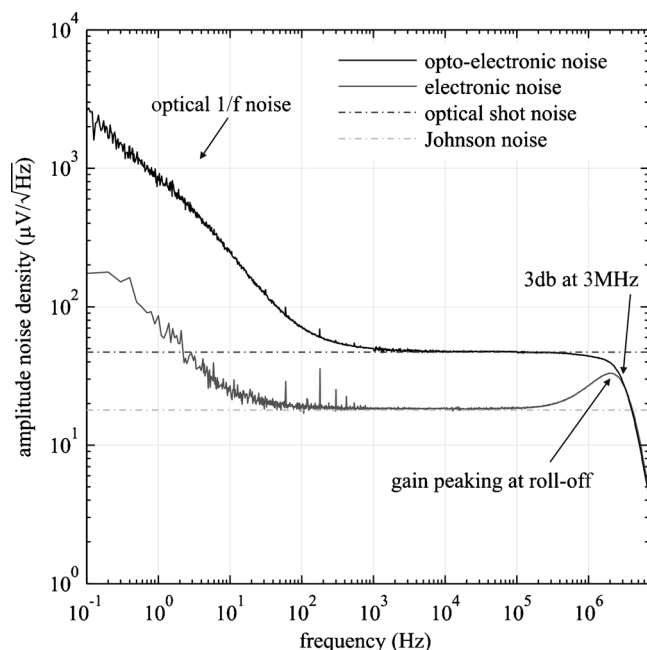


FIG. 8. Measured optoelectronic noise density and electronic noise density, together with the calculated optical shot noise density and electronic Johnson noise density. Optical noise dominates the optoelectronic noise across the usable bandwidth of the friction force microscope. Gain peaking at the 3 MHz roll-off is below the shot noise level.

the scanner's lowest resonance frequency, the normal and lateral force signals hold valuable tribological information extending beyond the imaging bandwidth. For example, fast measurements of stick-slip motion have revealed information about multiple contact formation during slip events.<sup>15</sup>

The temporal resolution of the cantilever deflection is ultimately limited by the bandwidth of the first stage of photodetection: the photocurrent amplifier. The bandwidth of an active photocurrent amplifier is determined by the geometric mean of the gain-bandwidth-product (GBP) of the operational amplifier and the low-pass frequency of the RC equivalent circuit.<sup>16</sup> The LT1214 operational amplifier was chosen for its compromise between a high GBP of 28 MHz and low  $1/f$  current and voltage noise. The optimal transimpedance feedback resistor and capacitor values were determined as 20 k $\Omega$  and 5 pF, which attained a 3 MHz detection bandwidth without compromising resolution and avoiding significant *gain peaking* at this roll-off frequency. After further amplification ( $531\times$ ), the lateral force signal is acquired by means of a high-speed digitizer (PCI-5122, National Instruments).

The *optoelectronic noise* and bandwidth were quantified by shining the collimated light beam directly at the photodetector. For a relevant characterization, the optical power impinging on the photodetector was adjusted to 320  $\mu\text{W}$ , which is typical for the light reflected off a cantilever. The noise density of this signal is the *optoelectronic noise density*. It is shown in Fig. 8, where the 3 dB roll-off at 3 MHz is visible and the  $1/f$  noise dominates *shot noise* for frequencies below 1 kHz. Figure 8 also depicts the *electronic noise* alone (with the light switched off) and its main source: *Johnson noise*. The electronic noise makes only a minor contribution (<10%) throughout the relevant bandwidth. The

*optomechanical noise*, representing any mechanical noise between the optoelectronics and the cantilever base, was tested by reflecting the light beam off the rigid cantilever base; its contribution was undetectable. In conclusion, the OBD *optical detection noise*  $n_{\text{OD}}$  is dominated by the *optical noise* of the light beam:  $1/f$  noise at low frequencies and shot noise at high frequencies.

Finally, the *angular detection noise*  $n_{\theta}$  (rad/ $\sqrt{\text{Hz}}$ ) fully describes the precision of the OBD system. It is the calibrated version of  $n_{\text{OD}}$  (V/ $\sqrt{\text{Hz}}$ ). The calibration factor is the *angular deflection sensitivity*  $S_{\theta}$  (V/rad), which is proportional to the divergence of the light beam reflected off the cantilever.<sup>17</sup>

## B. Lateral and normal force noise

The next step in the noise characterization is the conversion of the angular detection noise density  $n_{\theta}$  (rad/ $\sqrt{\text{Hz}}$ ) into a force detection noise density (N/ $\sqrt{\text{Hz}}$ ) for a given cantilever using the factor of  $3/2lk_N$  for normal force and  $hk_L$  for lateral force, discussed in Sec. II E. They carry units of N/rad. Figure 9(a) shows the calibrated normal force detection noise  $n_{\theta-N}$ . The *tip-sample noise*  $n_{\text{TS-N}}$  cannot be measured separately, but it can be deduced by acquiring the *in-contact noise*  $n_{\text{IC-N}}$  and quadratically subtracting the normal force detection noise:  $n_{\text{TS-N}}^2 = n_{\text{IC-N}}^2 - (\frac{3}{2}lk_N \cdot n_{\theta})^2$ . This is apparent in Fig. 7. The in-contact noise  $n_{\text{IC-N}}$  is measured by bringing the FFM tip into contact with a flat gold terrace and switching off the feedback controller.

The analogous result for the lateral signal is shown in Fig. 9(b). Notable sources of tip-sample noise are the *piezoelectric tube vibrations*, the *thermal resonance modes* of the cantilever, and *noise coupling through the liquid inlet/outlets*.

## C. Imaging performance

*Scanning noise*, from Fig. 7, is difficult to systematically quantify as it refers to any noise or unwanted signal which arises only during imaging. It has thus far not been mentioned because of its strong dependence on operating conditions rather than FFM design and has many potential sources: tip changes, disruption caused by contaminants, hydrodynamics from sample movement, scanning induced adsorption/desorption around the contact, etc.

Figure 10 depicts a lateral force map of a Au(111) surface at a normal load of 0.0 nN in 0.1 M HClO<sub>4</sub> at an open-circuit potential of 200 mV. It was chosen because the herringbone reconstruction is at the limit of instrumental lateral resolution. The patches are  $\sim 2$  Å deep corrosion pits remaining from an oxidation-reduction cycle of the surface. The lateral force peak-to-peak contrast caused by the herringbone structure starts at 25 pN at the bottom of the image and fades as the scan progresses. Near the top, it is dominated by noise with a standard deviation of 30 pN. This noise value is dominated by in-contact noise of the instrument, which suggests that the scanning noise is negligible in this case. Nearly half of this noise was aliased shot noise and lateral cantilever resonances in the >10 kHz bandwidth. This could have been avoided by using an antialiasing filter

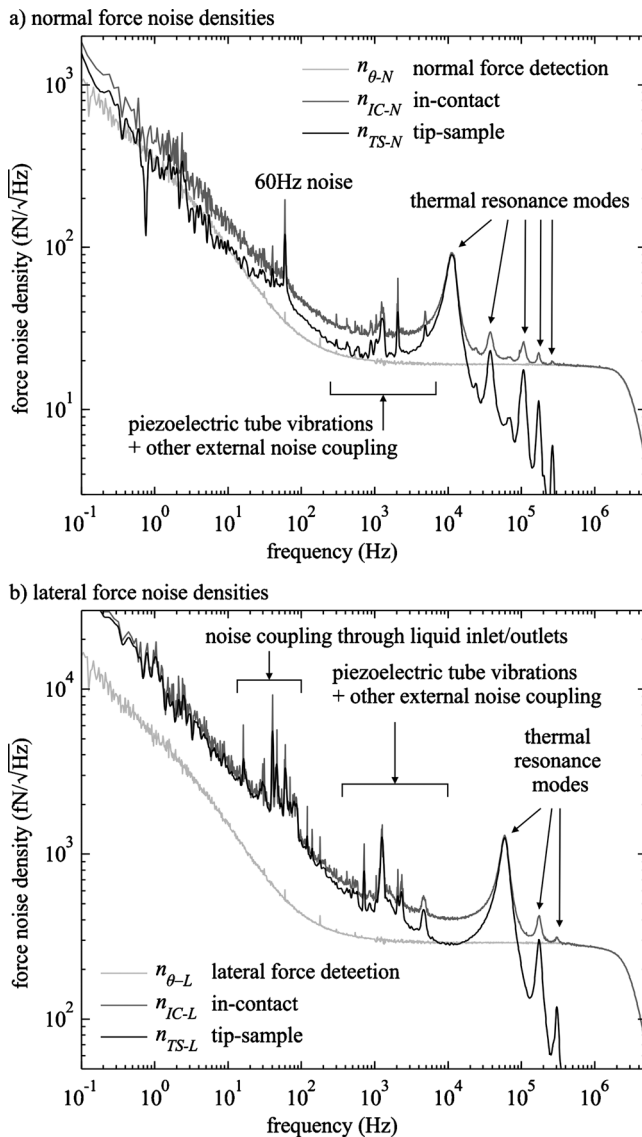


FIG. 9. In-contact lateral and normal force noise densities broken down into their two components: detection noise and mechanical noise (tip-sample). The in-contact noise density was acquired by putting the tip into contact with a Au(111) surface at low load ( $<1$  nN). The detection noise density was measured by pointing the light beam directly at the photodetector (with the optical power matched to the first dataset). The tip-sample mechanical noise was calculated by quadratic subtraction of the first two spectra. See the noise roadmap in Fig. 7.

for the lateral signal (before the controller input) with a 10 kHz cutoff, which is half the sampling frequency used in Fig. 10. It is important to realize that not all commercial AFM controllers implement an antialiasing filter, which is adapted to the actual sampling frequency.

The stability of the instrument in the XY plane is demonstrated in Fig. 11 by the atomic-scale lateral force map of a Au(111) surface in  $0.1$  M  $\text{HClO}_4 + 10^{-5}$  M  $\text{HCl}$ . A line profile shows the stick-slip behavior of the tip with an amplitude of  $2.5$  nN. The friction force per line averages to  $120$  pN with a measured standard deviation of  $24$  pN across the image. Below  $0.1\%$  of this standard deviation is caused by in-contact noise, while one-third is caused by the corrugation of the lattice in the slow-scan (vertical) direction. This occurs because the lattice is in registry with the fast scan

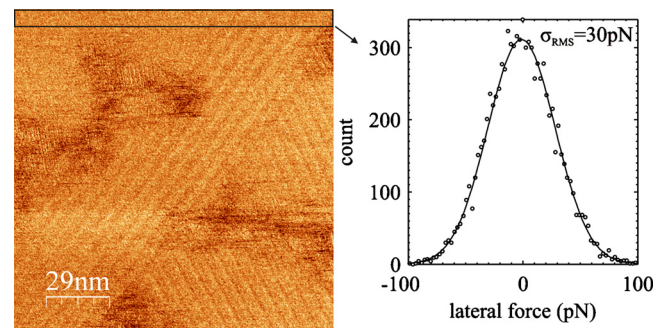


FIG. 10. (Color online) (a) Lateral force map of the herringbone reconstruction of Au(111) in  $0.1$  M  $\text{HClO}_4$  recorded at an open circuit potential of  $200$  mV. Image was flattened. (b) Histogram of boxed region shows the noise resolution of the herringbone signal. This  $30$  pN noise corresponds to the in-contact noise of the system, which is dominated by optical shot noise.

direction.<sup>18</sup> The rest of the variations in friction originate from physically detectable tip movements. Such variations would fall under the scanning noise category in Fig. 7, as they are caused by unwanted changes in the tip-sample junction. It is worth reiterating that although the tip-sample noise does not cause any significant noise preventing the detection of friction, its high frequency components (mainly cantilever thermal vibrations and piezoelectric tube vibrations) can significantly affect the friction signal and its variations within the low-frequency bandwidth of the measurement. Responsible mechanisms for such tribological behavior are the object of many studies.<sup>19,20</sup>

#### D. Time-resolved stick-slip

In studying the stick-slip phenomenon, the physics of interest lie in the dynamics of the tip-sample contact, with relevant parameters being the lateral force and the displacement between the tip apex and the sample surface. The tip apex and samples surface are connected by a mechanical

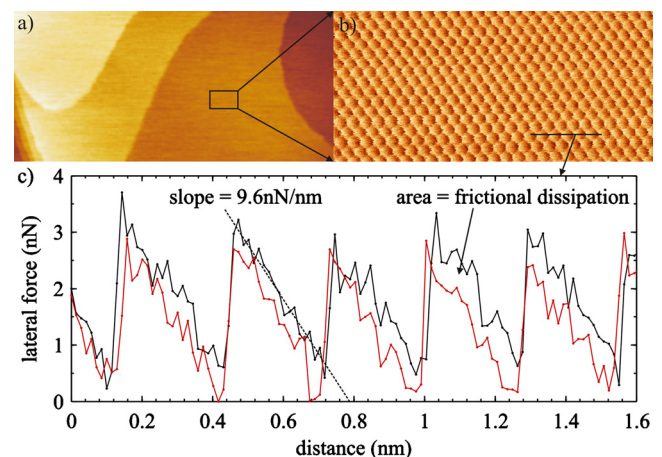


FIG. 11. (Color online) (a)  $600 \times 280$  nm<sup>2</sup> topography image of monatomic steps on Au(111). Image was flattened. (b) Lateral force map of the Au(111) lattice ( $25$  lines/s; normal load of  $15$  nN). The image was not filtered. (c) Backward and forward line profiles taken from (b) (pixel sampling frequency  $25.6$  kHz). The area in between both curves equals the frictional dissipation energy. The slope can be used to measure of the contact stiffness. Images recorded in  $0.1$  M  $\text{HClO}_4$  with trace chloride impurities at an EC potential of  $350$  mV.

loop which includes the cantilever—the force transducer. The torsional bending of the cantilever is used as a measure of the lateral force. However, other elements of the mechanical loop are not infinitely stiff and play an important role in the atomic stick-slip measurement. Both the in-plane bending of the cantilever and the tip compliance can have stiffnesses on the same order as the torsional bending.<sup>21,22</sup> The measurement of the tip apex position is not straightforward because the lateral displacement of the mechanical loop is divided among all these springs in series, whereas the OBD system only measures one of them: the torsional bending of the cantilever. The work of Sader and Green predicts a ratio of 1.0 between the in-plane and torsional bending of the cantilever used here.<sup>22</sup> This implies that the OBD system records only half of the lateral tip displacement. Furthermore, the tip compliance can become another significant source of error depending on the tip radius and normal load, as demonstrated by Lantz *et al.*<sup>21</sup> In principle, for quasistatic measurements, knowledge of all stiffnesses allows one to determine the true tip apex position and therefore the true contact stiffness.<sup>23</sup>

The lateral force detection is simplified by the fact that springs in series all have an equal applied force. After proper cantilever calibration, discussed in Sec. II E, the lateral OBD signal can be assigned accurate units of nN. However, this calibration is only valid for quasistatic forces; it is inaccurate for higher bandwidth measurements approaching the frequency of the first lateral resonance mode and meaningless for higher frequencies. The torsional response of the cantilever to lateral forces is governed by the cantilever's transfer function, which is frequency dependent and nonmonotonic. Interpretation of signals around or above the first resonance requires special consideration, such as derived by Yurtsever *et al.*<sup>24</sup> For a sudden change in lateral force, the frequency response of the cantilever peaks at the resonance and then rolls off as the inertia of the cantilever limits force detection. As such, the units of  $N/\sqrt{\text{Hz}}$  assigned in Fig. 9 to the thermal resonances should be regarded as noise sources calibrated according to how they corrupt quasistatic force measurements—such as in the aliasing example from the previous section.

Even though the inertia of the cantilever rolls off the force response above its first resonance, fast displacements of the tip apex can be detected by the OBD system. However, another level of complexity arises in the calibration of fast stick-slip measurements of the tip apex position. The effective stiffnesses of the three springs in series may vary greatly as a function of frequency with respect to each other. For example, exciting the second torsional flexural mode requires more pronounced twisting of the cantilever for a given lateral displacement amplitude and therefore a larger effective stiffness. Therefore, the calibration factor, which combines all the stiffnesses in series, will be highly frequency dependent. For example, the stiffness of the tip apex cluster can be considered constant up to gigahertz frequencies,<sup>25</sup> whereas the effective lateral stiffness of the cantilever will increase for higher flexural modes. Although the calibration factor for high frequencies is difficult to determine, it remains desirable to collect the OBD data at frequencies above

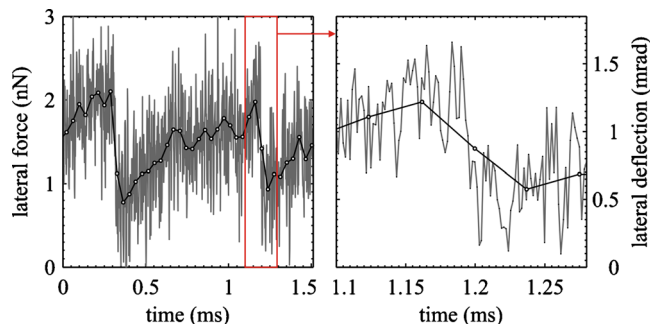


FIG. 12. (Color online) (a) Grey: stick-slip data acquired at a sampling frequency of 606 kHz. Black: averaged data to mimic data acquisition at 25.6 kHz of the AFM controller during typical imaging. The slowly sampled data is assigned accurate units of nN. (b) Zoom-in showing the 1.65  $\mu\text{s}$  data sampling (606 kHz) by the high-speed digitizer. The axis was left in the native measurement units (mrad) to avoid the complicated interpretation of forces and displacements for fast tip-sample contact dynamics.

the first resonance and up to the limit of shot noise because they provide further insight into the dynamics of the tip-sample contact.

Figure 12(a) displays stick-slip data on Au(111) in 0.1 M  $\text{HClO}_4 + 10^{-5}$  M HCl. The black curve can be assigned units of nN because its effective sampling rate is below the first lateral resonance frequency. Figure 12(b) is a zoom-in which shows the raw OBD data acquired with a sampling frequency of 606 kHz. The units of the signal were left in their native OBD units (rad) because the sampling frequency exceeds the first resonance of 58 kHz, thereby rendering the first order force calibration inaccurate. This fundamental limit for lateral force timing resolution can only be improved by using a cantilever with a higher lateral resonance frequency or, to a certain degree, by modeling the transfer function of the complete cantilever-tip system.

## E. Liquid confinement

In this section, the first normal thermal resonance is used as a signal to probe the liquid structure of OMCTS near a highly oriented pyrolytic graphite (HOPG) surface. Liquid confinement refers to the ordering of liquids perpendicular to the surface when constrained between two solids separated by distances on the order of nanometers. This phenomenon can be detected with an AFM tip acting as one of the surfaces: the oscillatory forces attempt to maintain a tip-to-surface distance that is an integer multiple of liquid layers. Consequently, recording the tip position while moving the surface toward the cantilever allows the reconstruction of the energy landscape of liquid confinement because the relative occupancy of states is related to energy through Boltzmann statistics.

Figure 13(a) shows the tip-surface separation during an approach of 3 nm/s using a silicon cantilever with normal stiffness of 0.11 N/m. The layering is visible as a steplike distribution of tip-sample distances for up to three layers of OMCTS at 0.9 nm per layer. At distances above 2 nm, thermal motion of the cantilever dominates the layering because the effective energy barrier between layers falls below  $k_B T$ . In this regime, the system can be considered in thermal equi-

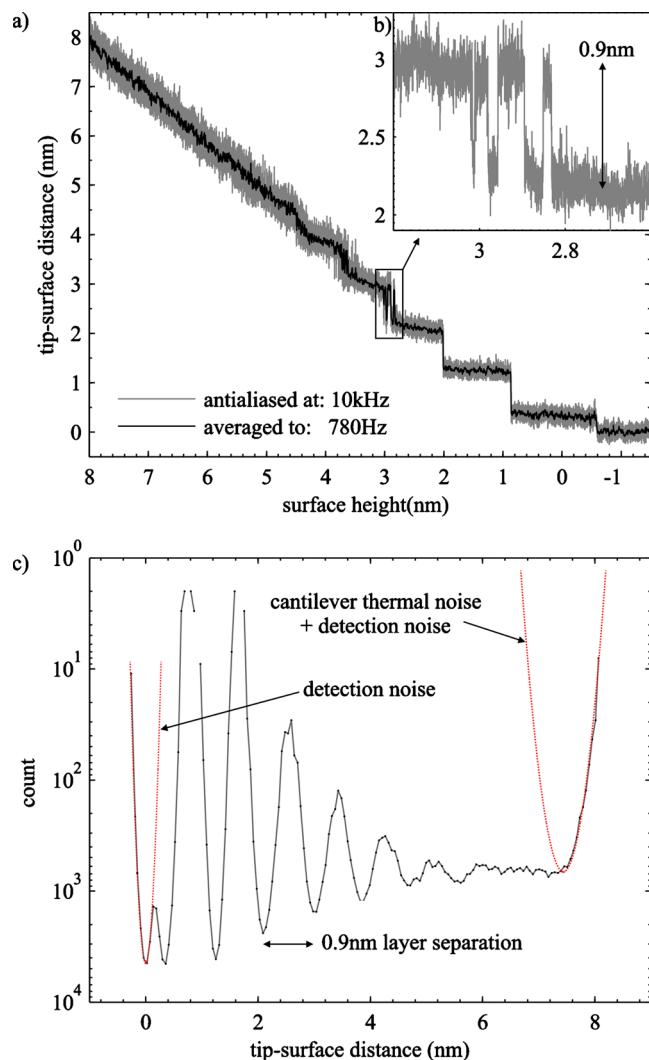


FIG. 13. (Color online) (a) Approach curve of a cantilever tip toward a graphite (HOPG) surface in OMCTS. The inset shows stochastic motion of the cantilever tip jumping back and forth between two OMCTS layers. The sampling rate is 40 kHz. (b) Histogram of the relative occupancy of tip-surface distances in the curve in (a). The inverted logarithmic plot visually represents the energy landscape which is exponentially related to the relative occupancy of tip-surface distances.

librium where the stochastic motion of the tip samples the combined solvation potential and cantilever potential. Figure 13(b) exemplifies this behavior.

Cleveland *et al.* pioneered the method of using thermal motion of the cantilever to probe the solvation potential near a solid interface.<sup>26</sup> Tip-sample distances are binned throughout the approach in order to reveal the basic structure of the energy landscape. In the histogram in Fig. 13(c), seven layers of OMCTS can be readily distinguished. The actual solvation potential is convolved by the *cantilever harmonic potential* and noise. As the tip approaches the sample, the detection noise stays constant whereas the mechanical noise varies from layer to layer. The first thermal resonance mode decays as the tip penetrates each layer due to the increasing tip-sample stiffness; the layers can be thought of as springs in series. The energy landscape becomes inaccurate for the first few layers because the system is not in thermal equilibrium: instabilities occur when the stiffness of the layers is higher

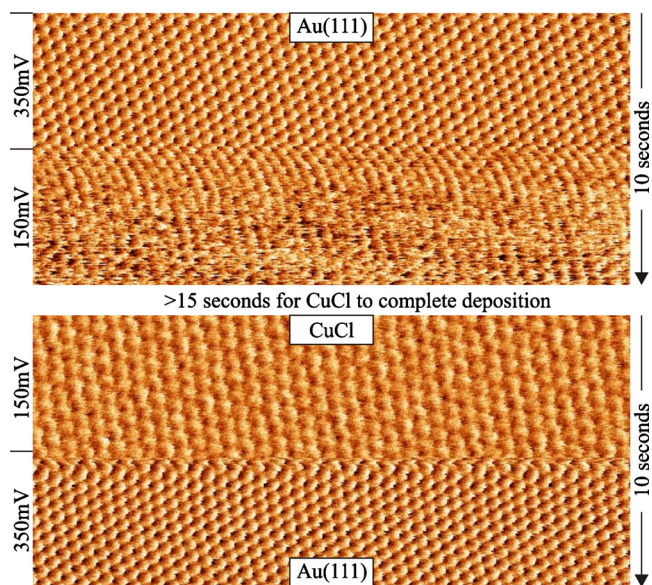


FIG. 14. (Color online) Lateral force map of the deposition and desorption of CuCl on the Au(111) surface in 0.1 M HClO<sub>4</sub>+1.5 mM Cu(ClO<sub>4</sub>)<sub>2</sub>+10<sup>-5</sup> M HCl (normal load 2.0 nN, scanning at 25 lines/s). The switching of the sample potential (vs Ag/AgCl) is indicated on the left. Lattice spacings: CuCl 3.67 Å and Au(111) 2.88 Å. Average friction for CuCl covered and Au(111) surfaces:  $f_{\text{Cu}}=100$  pN,  $\sigma_{\text{Cu}}=20$  pN;  $f_{\text{Au}}=240$  pN,  $\sigma_{\text{Au}}=30$  pN.

than the stiffness of the cantilevers and the thermal fluctuations of the cantilever are too small to sample across the different layer configurations repeatedly.

#### IV. ATOMIC FRICTION UNDER ELECTROCHEMICAL CONTROL

A well studied electrochemical system was chosen for the first friction experiment: Cu UPD on Au(111) in perchloric acid.<sup>27</sup> The goal is to study relative tribological differences between atomically flat Au(111) and a Cu UPD monolayer in liquid environment. By quickly and reversibly switching between both surfaces, systematic errors caused by tip changes and drift can be greatly reduced or at least identified.

The addition of trace amounts of chloride (10<sup>-5</sup> M) to this system is necessary for two reasons. The oxidation-reduction cycles used in the electrochemical preparation of the atomically flat Au(111) surface require chloride to increase the mobility of the gold atoms;<sup>28</sup> otherwise, unrecoverable corrosion pitting occurs as seen in Fig. 10. Second, chloride is required for Cu UPD in perchloric acid, which occurs by coadsorption into the formation of a CuCl(111)-like bilayer.<sup>28</sup>

Figure 6 shows the cyclic voltammogram after the addition of copper percholate (1.5 mM) to the 0.1 M HClO<sub>4</sub>+10<sup>-5</sup> M HCl solution. Switching the potential from 350 to 150 mV induces reversible Cu UPD, as seen by the change in surface structure in the lateral force maps in Fig. 14. The instability on the order of seconds during deposition can be attributed to the slow deposition kinetics and the disruption caused by the scanning tip.

The large lattice mismatch between both surfaces implies that the copper binds more strongly with chloride than

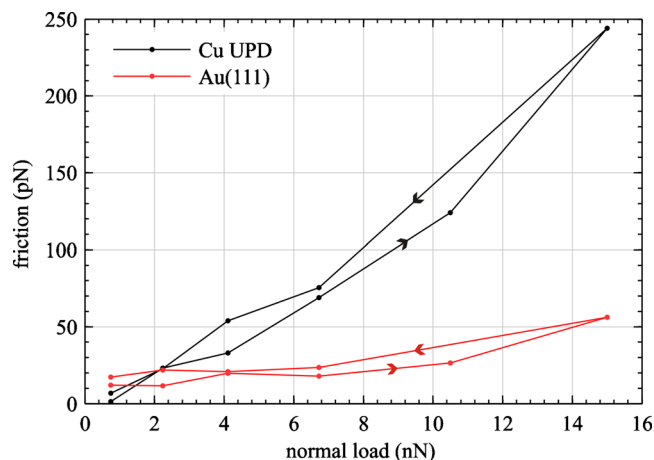


FIG. 15. (Color online) Friction force vs normal load on Au(111) and Cu UPD layer. The adhesion is found to be 0.6 and 1.2 nN, respectively, in pull-off experiments. The arrows indicate the order of the data acquisition. Both surfaces were alternated at every normal load value.

with gold. While there is only a small difference in lattice spacing between Cu(111) and Au(111) (2.56 Å versus 2.88 Å), the Cu UPD lattice constant of 3.67 Å in Fig. 14 is close to the CuCl bulk value of 3.82 Å.<sup>28</sup>

The friction plot in Fig. 15 depicts the friction force as a function of normal load on both surfaces far from any step edges. All the data were acquired consecutively in order to easily correct for drift and identify any large tip changes that can render the experiment inaccurate. The repeatability of the data was confirmed by ramping the normal load back down in the second half of the experiment. Furthermore, the changing of the normal load and the switching between surfaces were alternated to make the relative comparison in friction more accurate. Each data point in Fig. 15 represents 2048 friction data points averaged over 100 s at a specific normal load and surface; 25 s of data were discarded after each transition to avoid the effects of transients. The variability of the data is completely dominated by the scanning noise discussed earlier. Continuous changes of the atomic geometry and composition of the tip-sample contact are the most probable origin of this scanning noise.

At high normal loads, the friction on the CuCl layer is consistently larger than on Au(111). This increase in friction occurs well below the onset of wear, which can be identified by a sudden jump in dissipation and simultaneous degradation of the visual quality in stick-slip imaging. Onset of wear can be attributed to a penetration of the scanning tip through either the Cl overlayer or through the full CuCl layer. Given the strong bonding between Cu and Cl, the latter situation seems more likely.

At low normal loads, most datasets present a crossover region, where the Au(111) exhibits larger friction than the CuCl layer below a certain normal load. This might be due to the adhesion on Au(111) which is found in pull-off experiments to be 30%–80% larger than on the CuCl layer. However, all control experiments on Au(111) without any copper in the solution also show a systematically larger friction at 350 mV than at 150 mV, despite a constant adhesion at both potentials in this case. Thus, the cause of this crossover is

uncertain: it can be any combination of true material contrast of friction, change in adhesion, or a potential-induced change in the double layer structure and adsorbate composition.

## V. SUMMARY

The design and development of an atomic-scale electrochemical FFM were presented. The design choices were justified with regard to the requirement of both a stable tip-to-sample mechanical junction, as well as a clean, stable, and electrochemically controllable environment. The noise of the system was analyzed by the proposed step-by-step process led by Fig. 7 which represents a breakdown of all the FFM noise sources and their propagation into the final measurement. Then, the performance of the FFM was demonstrated on a series of lateral force experiments, where the limiting factors in each were discussed with respect to results from the noise analysis. The frequency dependent response of the cantilever was also discussed as a limiting factor for fast force detection, such as in atomic stick-slip. The normal force detection was demonstrated in a study of the solvation potential of OMCTS. Lastly, a comparative study between bare Au(111) and a Cu UPD monolayer in perchloric acid was performed; atomic stick-slip on both surfaces was observed in a single FFM image. While the friction on Cu UPD is lower at low normal loads (<2 nN), it has much stronger dependence on normal load and greatly exceeds the friction on Au(111) for high loads.

## ACKNOWLEDGMENTS

The authors would like to thank Bill Ho for his advice in the initial phase of this project. Financial support by the Canada Foundation for Innovation (CFI) and the National Sciences and Engineering Research Council (NSERC) is gratefully acknowledged.

- <sup>1</sup>C. M. Mate, G. M. McClelland, R. Erlandsson, and S. Chiang, *Phys. Rev. Lett.* **59**, 1942 (1987).
- <sup>2</sup>E. Riedo, F. Lévy, and H. Brune, *Phys. Rev. Lett.* **88**, 185505 (2002).
- <sup>3</sup>M. Dienwiebel, G. S. Verhoeven, N. Pradeep, J. W. M. Frenken, J. A. Heimberg, and H. W. Zandbergen, *Phys. Rev. Lett.* **92**, 126101 (2004).
- <sup>4</sup>M. Binggeli, R. Christoph, H. E. Hintermann, and O. Marti, *Surf. Coat. Technol.* **62**, 523 (1993).
- <sup>5</sup>M. Niellinger and H. Baltruschat, *Phys. Chem. Chem. Phys.* **9**, 3965 (2007).
- <sup>6</sup>F. Hausen, M. Niellinger, S. Ernst, and H. Baltruschat, *Electrochim. Acta* **53**, 6058 (2008).
- <sup>7</sup>A. Socoliuc, R. Bennowitz, E. Gnecco, and E. Meyer, *Phys. Rev. Lett.* **92**, 134301 (2004).
- <sup>8</sup>G. Meyer and N. M. Am, *Appl. Phys. Lett.* **53**, 1045 (1988).
- <sup>9</sup>T. E. Schäffer, J. P. Cleveland, F. Ohnesorge, D. A. Walters, and P. K. Hansma, *J. Appl. Phys.* **80**, 3622 (1996).
- <sup>10</sup>J. B. Thompson, B. Drake, J. H. Kindt, J. Hoskins, and P. K. Hansma, *Nanotechnology* **12**, 394 (2001).
- <sup>11</sup>Y. Golan, L. Margulis, and I. Rubinstein, *Surf. Sci.* **264**, 312 (1992).
- <sup>12</sup>D. Sarid, *Exploring Scanning Probe Microscopy with MATHEMATICA* (Wiley, New York, 1997).
- <sup>13</sup>J. E. Sader, J. W. M. Chon, and P. Mulvaney, *Rev. Sci. Instrum.* **70**, 3967 (1999).
- <sup>14</sup>C. P. Green, H. Lioe, J. P. Cleveland, R. Proksch, P. Mulvaney, and J. E. Sader, *Rev. Sci. Instrum.* **75**, 1988 (2004).
- <sup>15</sup>S. Maier, Y. Sang, T. Filleter, M. Grant, R. Bennowitz, E. Gnecco, and E. Meyer, *Phys. Rev. B* **72**, 245418 (2005).

- <sup>16</sup>J. G. Graeme, *Photodiode Amplifiers: Op Amp Solutions* (McGraw-Hill, New York, 1995).
- <sup>17</sup>B. Bhushan, *Springer Handbook of Nanotechnology*, 2nd ed. (Springer, Berlin, 2005).
- <sup>18</sup>A. Schirmeisen, L. Jansen, and H. Fuchs, *Phys. Rev. B* **71**, 245403 (2005).
- <sup>19</sup>M. A. Lantz, D. Wiesmann, and B. Gotsmann, *Nat. Nanotechnol.* **4**, 586 (2009).
- <sup>20</sup>R. Guerra, A. Vanossi, and M. Urbakh, *Phys. Rev. E* **78**, 036110 (2008).
- <sup>21</sup>M. A. Lantz, S. J. Oshea, A. C. F. Hoole, and M. E. Welland, *Appl. Phys. Lett.* **70**, 970 (1997).
- <sup>22</sup>J. E. Sader and C. P. Green, *Rev. Sci. Instrum.* **75**, 878 (2004).
- <sup>23</sup>R. W. Carpick, D. F. Ogletree, and M. Salmeron, *Appl. Phys. Lett.* **70**, 1548 (1997).
- <sup>24</sup>A. Yurtsever, A. M. Gigler, E. Macias, and R. W. Stark, *Appl. Phys. Lett.* **91**, 253120 (2007).
- <sup>25</sup>S. Y. Krylov and J. W. M. Frenken, *New J. Phys.* **9**, 398 (2007).
- <sup>26</sup>J. P. Cleveland, T. E. Schäffer, and P. K. Hansma, *Phys. Rev. B* **52**, R8692 (1995).
- <sup>27</sup>E. Herrero, L. J. Buller, and H. D. Abruna, *Chem. Rev. (Washington, D.C.)* **101**, 1897 (2001).
- <sup>28</sup>J. Hotlos, O. M. Magnussen, and R. J. Behm, *Surf. Sci.* **335**, 129 (1995).